Puffin Platform: A Morphable Unmanned Aerial/Underwater Vehicle With Eight Propellers

Hongxia Rao, Lijie Xie, Jiapeng Yang, Yong Xu, *Member, IEEE*, Weijun Lv, Zongkai Zheng, Yihui Deng, and Haotian Guo

***Abstract*—In this article, a morphable unmanned aerial/underwater vehicle with eight propellers named Puffin platform is investigated. To improve the efficiency of rotor utilization underwater, a tilting mechanism is designed, where the direction of rotors can be changed. As tilting the rotors causes severe underactuation of the vehicle, an attitude control method is proposed. In addition, an adaptive controller is designed for trajectory tracking, and the stability analysis is analyzed by the Lyapunov-like lemma. Simulations are then used to verify the performance of the control strategy. Finally, we assemble the Puffin platform and conduct preliminary experiments to demonstrate its performance in the air, underwater, and during transition.**

***Index Terms*—Attitude control, motion control, unmanned aerial vehicles (UAVs).**

Nomenclature

$\mathbf{P}(\Phi_1) \in \mathbb{R}^{3\times3}$	Transformation matrix from the body fixed angular rate to the Euler angles rate.
$\mathbf{R} \in \mathbb{R}^{3\times3}$	Rotation matrix from the body fixed frame to the inertial frame.
$\times$	Multiplication cross.
$J \in \mathbb{R}^{3\times3}$	Inertia matrix.
$D_\phi \in \mathbb{R}^{3\times3}$	Diagonal matrix with absolute value elements.
γ	Trigonometric diagonal matrix.
ESC	Electronic speed controllers.
BLDC	Brushless direct current.
PWM	Pulsewidth modulated.
BEC	Battery elimination circuit.
SBUS	Serial bus.

Manuscript received 6 June 2023; revised 3 August 2023; accepted 16 August 2023. Date of publication 11 September 2023; date of current version 29 February 2024. This work was supported in part by Key Area Research and Development Program of Guangdong Province under Grant 2021B0101410005, in part by the National Natural Science Foundation of China under Grant 62121004, Grant U22A2044, and Grant 62006043, in part by the Local Innovative and Research Teams Project of Guangdong Special Support Program under Grant 2019BT02X353, and in part by the Natural Science Foundation of Guangdong Province, China under Grant 2021B1515420008. *(Corresponding author: Yong Xu.)*

Hongxia Rao, Lijie Xie, Jiapeng Yang, Yong Xu, Weijun Lv, and Haotian Guo are with the Guangdong Provincial Key Laboratory of Intelligent Decision and Cooperative Control, School of Automation, Guangdong University of Technology, Guangzhou 510006, China (e-mail: raohxia@163.com; xielijie_gdut@163.com; waxywaxy@outlook.com; yxu@gdut.edu.cn; lvweijun1997gdut@163.com; guohaotian@gdut.mail2.edu.cn).

Zongkai Zheng is with the Department of Mechanical Engineering and Automation, Harbin Institute of Technology, Shenzhen 518055, China (e-mail: zongkaizheng@163.com).

Yihui Deng is with the Department of Electronic Information Engineering, University of Electronic Science and Technology of China, Sichuan 611731, China (e-mail: yihuideng@std.uestc.edu.cn).

Color versions of one or more figures in this article are available at https://doi.org/10.1109/TIE.2023.3310025.

Digital Object Identifier 10.1109/TIE.2023.3310025

I. Introduction

In RECENT years, unmanned aerial vehicles (UAVs) have been widely applied in many fields, such as rescue, monitoring, tracking, and so on [1], [2], [3]. With the increasing complexity of application scenarios, more functionalities are required for UAVs, such as vertical takeoff and landing (VTOL) UAV [4], unmanned system collaboration [5], [6], [7], and unmanned hybrid systems [8], [9]. Among the unmanned hybrid systems, unmanned aerial/underwater vehicles (UA/UVs) have received increasing attention [10], since they are adequate for more complex tasks in different environments.

Previously developed UA/UVs can be classified into two categories according to their configurations: multirotor configuration and fixed-wing configuration. In order to optimize the performance of the vehicle in both air and underwater, many researchers studied the vehicle's design. Equipped with four aerial propellers and four aquatic propellers, hybrid unmanned aerial underwater vehicles (HUAUVs) achieved efficient underwater propulsion [11]. To fly in different mediums only using the aerial propellers, a ballast system was used to control the vehicle buoyancy [12], [13]. Furthermore, an octo-quadcopter configuration was introduced for better transition in [14]. These multirotor UA/UVs are maneuverable and controllable, however, they are not efficient in rotor utilization. For comparison, the submersible-launching UA/UVs have long endurance because the rotors are solely used for propulsion [15], [16], [17], but they need to build up the speed prior to transition. Moreover, the differences in the density of the mediums should be considered, which makes the design of wings challenging.

To further improve flight capabilities and efficiency, some researchers tried to mix the configuration of multirotor UAV with fixed-wing UAV. The hybrid VTOL UAV has the extra propulsion [18]. The tilt-wing aircraft system just tilts some of the wings [19]. Such a configuration also helps to improve the

performance of UA/UVs. The NEZHA merged the design of the fixed-wing UAV, the multirotor UAV, and the underwater glider (UG) [20]. However, its structure and control are complex since a lightweight pneumatic buoyancy adjustment system is used to control the altitude underwater. The morphable multimodal quadrotor used a morphable vehicle structure to improve the balance of aerial-aquatic performance [21]. But the utilization of the underwater thrust is not efficient because the tilting direction of the rotors for propulsion is not forward. However, this vector thrust design is instructive, which helps to improve the flight efficiency of the vehicle underwater.

To this end, we develop the puffin platform, an octo-quadcopter vehicle in "+8" configuration equipped with a tilting mechanism. The tilting mechanism transforms the rotors into two independent propulsions for the buoyancy and translational motion control of the platform, respectively. Thus, the vehicle can effectively move underwater without pitching or rolling at a large angle. Moreover, this design is useful for localization because the direction of the sensors for localization such as cameras [22], [23] and pressure sensors [24] would not be affected by body rotations.

A challenge for an UA/UV with a novel structure is how to design the flight control strategy. Existing UAVs mainly designed the controllers based on their dynamics model, which relies on an understanding of the physics of flight [25]. Based on the dynamic model of the conventional multirotor vehicle [26], the effects of drag, buoyancy, and Coriolis force underwater were considered in the modeling of the Naviator [14]. For the attitude control, a proportional integral derivative (PID) controller was used in [14] and [20]. To solve the severe underactuation of the vehicle after tilting the rotors, we design an attitude control method based on PID controller. For the position control, Naviator used a feedback linearization control law [14]. However, this method needs to know the density of water if the vehicle needs to work in different environments such as the lake and the sea. Therefore, we designed an adaptive control law to cope with the changes. The main contributions of this work are stated as follows.

1) A novel configuration concept for UA/UV is proposed. The tilting mechanism improves the efficiency of the underwater propulsion to reduce the energy cost for the platform.
2) A tilting mechanism control strategy is proposed for the specialty of the platform's structure, and an adaptive control law is designed to realize the position control of the platform.
3) Finally, preliminary experiments on the attitude control and the transition control are set up to verify the performance of the platform.

II. Puffin Platform Design

A. Tilting Rotor Drone Design

The puffin platform is divided into two components, where the upper layer contains the power unit and buoy system, and the lower layer is the waterproof pressure vessel. As shown in Fig. 1, the power unit uses a coaxial rotor structure to guarantee

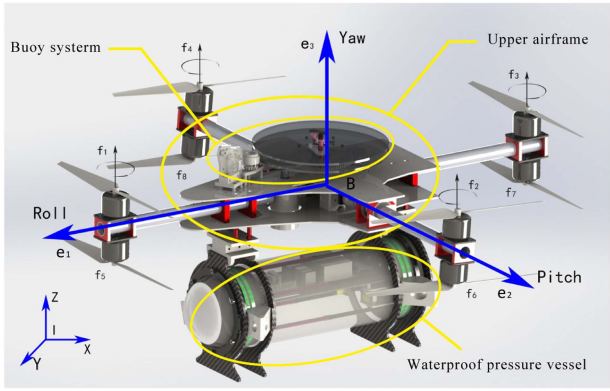

Fig. 1. Structure schematic of the Puffin platform.

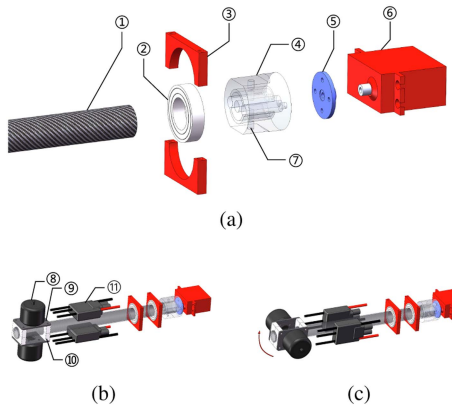

Fig. 2. Tilting rotor mechanism. (a) Diagram of decomposition. (b) Assembled mechanism. (c) Rotation of the mechanism.

the vehicle's stability when crossing the fluid boundary. Moreover, the implementation of the "+8" configuration permits the adjustment of the tilt angle for rotors on both sides. The upper airframe is composed of two 3 mm thick carbon fiber plates and four carbon fiber tubes. The tilting mechanism is equipped in the carbon fiber plates interlayer, and two brushless motors as well as ESCs [⑪ in Fig. 2(b)] are placed on the carbon fiber tubes. The axis distance of the fuselage is 55 cm on the roll axis and 60 cm on the pitch axis. The estimated moments of inertia of the platform around its roll, pitch, and yaw axes (via CAD software solidworks) are $J_x = 1.10 \times 10^6$, $J_y = 1.29 \times 10^6$, and $J_z = 2.06 \times 10^6$ g $\cdot$ cm^2, respectively. Finally, the waterproof pressure vessel in the lower layer is equipped with the electronic devices such as autopilot, receiver, and batteries.

B. Tilting Rotor Mechanism

Conventional UAVs need to rotate to the desired direction before translation motion. The flight drag increases because the cross-sectional area of the airframe in the direction of movement is changed. This drag is usually neglected in the air. However, it cannot be neglected underwater due to the higher density coefficient, which makes the vehicle's movement difficult. To

solve this problem, a tilting mechanism is designed in this work, where the left and right rotors become propulsion devices.

To achieve thrust vectoring underwater, the tilting mechanism is used to adjust the tilt angle of the rotors on both sides. The mechanism is decomposed in Fig. 2(a). It contains a carbon fiber tube [① in Fig. 2(a)], two bearings [② in Fig. 2(a)], a connector [④ in Fig. 2(a)], a disc rocker [⑤ in Fig. 2(a)] and a servo [⑥ in Fig. 2(a)]. The carbon fiber tube is externally nested by two bearings, and the bearings are supported by the metal bearing seats [③ in Fig. 2(a)] between the carbon fiber plates interlayer. This design allows the motors [⑧ in Fig. 2(b)] and the fixed components [⑨ and ⑩ in Fig. 2(b)] to rotate. In addition, as the main force-bearing components, the bearings make the drive components more durable. The rotation is activated by the servos, which are connected to the carbon tube through a connector made by nylon and a disk rocker. The connector contains a through-hole [⑦ in Fig. 2(a)] that can be penetrated with a screw to form a rigid connection with the carbon fiber tube. Finally, the assembled mechanism is shown in Fig. 2(b) and the rotation of the mechanism is shown in Fig. 2(c).

III. Dynamical Modeling

This platform has two modes of locomotion in diverse mediums: the air mode and the underwater mode. Although the structure of a vehicle changes in different modes, its attitude change can be regarded as the rotational motion of a rigid body around its axis. For the translational motion of the vehicle, the drive methods of two modes are different.

A. Attitude Dynamics

As show in Fig. 1, define a right-hand inertial frame $\mathbf{I} \triangleq \{X, Y, Z\}$, where the Z-axis is the vertical direction upwards to the earth. $\mathbf{B} \triangleq \{e_1, e_2, e_3\}$ stands for the body fixed frame of the vehicle. Due to the drag force can not be ignored underwater, the dynamic model of the designed vehicle can be obtained by the Newton–Euler equations

$$\begin{aligned} \dot{\Phi}_1 &= \mathbf{P}\Phi_2 \\ J\dot{\Phi}_2 &= \Gamma - \Phi_2 \times J\Phi_2 - C_{D_\phi}\rho D_\phi \Phi_2 \end{aligned} \tag{1}$$

where $\Phi_1 \triangleq [\phi \quad \theta \quad \psi]^T$, and ϕ, θ, ψ are the euler angles roll, pitch, and yaw, respectively. $\Phi_2 \in \mathbb{R}^3$ represents a body fixed angular velocity. $C_{D_\phi}\rho D_\phi \phi_2$ is the drag force, where C_{D_ϕ} denotes a diagonal drag coefficient matrix, and $D_\phi \triangleq diag\{|\dot{\phi}|, |\dot{\theta}|, |\dot{\psi}|\} \in \mathbb{R}^{3\times 3}$ is a diagonal matrix with absolute value elements. $\rho \in \{\rho_a, \rho_w\}$ stands for the density of the medium, where the air density $\rho_a \approx 1.2754\,\text{kg/m}^3$ and the water density $\rho_w \approx 1000\,\text{kg/m}^3$. $\Gamma \triangleq [\Gamma_\phi \quad \Gamma_\theta \quad \Gamma_\psi]^T \in \mathbb{R}^3$ denotes the input torque in roll, pitch, and yaw generated by the servos and the rotors, where the difference in rotor speed controls the magnitude of the torque, and the servos control the direction of the torque.

According to the generating methods of the torque, the input torque can be represented as

$$\Gamma = \boldsymbol{\gamma}\mathbf{T} + \mathbf{Q}$$

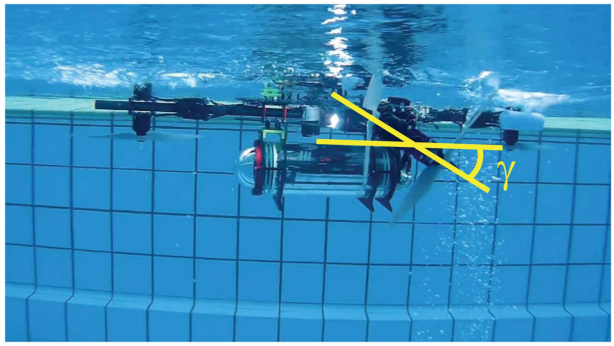

Fig. 3. Diagram of tilting rotor in underwater mode.

$$\mathbf{T} = \begin{cases} [T_{\phi,a} \quad T_{\theta,a} \quad T_{\psi,a}]^T, & \text{air mode} \\ [T_{\phi,w} \quad T_{\theta,w} \quad T_{\psi,w}]^T, & \text{underwater mode} \end{cases}$$

$$\mathbf{Q} = \begin{cases} [0 \quad 0 \quad Q_{\psi,a}]^T, & \text{air mode} \\ [0 \quad 0 \quad 0]^T, & \text{underwater mode} \end{cases} \tag{2}$$

where $\boldsymbol{\gamma} = \text{diag}\{\sin\gamma, 1, \cos\gamma\} \in \mathbb{R}^{3\times 3}$ denotes the trigonometric diagonal matrix that projects the thrust vector onto the basis vector. The vectors $\mathbf{T}$ and $\mathbf{Q}$ are the torque applied to the vehicle generated by thrust and reactive torque, respectively. Since the designed vehicle is a variable mode system, the torque Γ is generated in different ways in the air mode and the underwater mode.

1) Input Torque in Air Mode: For the air mode, the input torques are given by the combination of the thrust and the reactive torque

$$\begin{aligned} T_{\phi,a} &= l(\mathbf{f}_2^2 - \mathbf{f}_4^2 + \mathbf{f}_6^2 - \mathbf{f}_8^2) \\ T_{\theta,a} &= l(\mathbf{f}_1^2 - \mathbf{f}_3^2 + \mathbf{f}_5^2 - \mathbf{f}_7^2),\ T_{\psi,a} = 0 \\ Q_{\psi,a} &= kl(-\mathbf{f}_1^2 + \mathbf{f}_2^2 - \mathbf{f}_3^2 + \mathbf{f}_4^2 + \mathbf{f}_5^2 - \mathbf{f}_6^2 + \mathbf{f}_7^2 - \mathbf{f}_8^2) \end{aligned} \tag{3}$$

where $\mathbf{f}_i = \omega_i^2 \rho K$ stands for the thrust given by the rotors, and l is the distance from the rotor center to the mass center of the vehicle. The thrust $\mathbf{f}_i$ is related to the rotor's speed ω_i, the density ρ, and the rotor's constant K. The constant k stands for the mapping from the rotational speed of the rotor to its torque. In the air mode, the tilt angle $\gamma \in \{-90°, 90°\}$ of rotors (rotors 2, 4, 6, and 8) is set to be fixed at 90°. Under this mode, the torque Γ_ψ is given by the reactive torque $Q_{\psi,a}$.

2) Input Torque in Underwater Mode: For the underwater mode, the initial angle of the rotors mentioned above is set to be 0°. At this point, the rolling motion is achieved by tilting the rotors symmetrically and increasing the thrust. For example, the tilt angle of the left rotors (rotors 2 and 4) is set to be γ and right rotors (rotor 4 and 8) are set to be $-\gamma$ (see Fig. 3). Moreover, the top and bottom rotors rotate in opposite directions that the reactive torque of the rotors can be cancelled, which means that the mode $\mathbf{Q}$ is a zero vector. Noteworthy, the input torque in the yaw direction is given by the reactive torque of the rotors in the air mode, but it is produced by the thrust in the underwater mode. To summarize above, the input torques in the underwater

mode can be represented as

$$\begin{aligned} T_{\phi,w} &= l(\mathbf{f}_2^2 + \mathbf{f}_4^2 + \mathbf{f}_6^2 + \mathbf{f}_8^2) \\ T_{\theta,w} &= l(\mathbf{f}_1^2 - \mathbf{f}_3^2 + \mathbf{f}_5^2 - \mathbf{f}_7^2) \\ T_{\psi,w} &= l(-\mathbf{f}_2^2 + \mathbf{f}_4^2 - \mathbf{f}_6^2 + \mathbf{f}_8^2). \end{aligned} \tag{4}$$

B. Translation Dynamics

The translational motion of the designed vehicle is divided into two modes depending on the propulsion methods. In the air mode, the rotational motion of the vehicle is coupled with the translational motion. The vehicle needs to pitch or roll in the target direction and increase collective thrust to achieve translational motion. However, the motion can be decoupled in the underwater mode because the forward motion is drove by the left and right side rotors directly. For the up–down motion underwater, it is achieved by adjusting the value of thrust (rotors 1, 3, 5, and 7). Despite the different patterns of vehicle motion in different mediums, the translational dynamics of the vehicle can still be represented by a set of equations based on the coordinate system defined in the previous section

$$\begin{aligned} \dot{\xi}_1 &= \xi_2 \\ m\dot{\xi}_2 &= \mathbf{T}_1\mathbf{R}e_3 + \mathbf{T}_2\mathbf{R}e_1 - g(m - \rho V)e_3 - C_{D_\xi}\rho D_\xi \xi_2 \\ \mathbf{T}_1 &= \begin{cases} \sum_{i=1}^{8} \mathbf{f}_i, & \text{air mode} \\ \mathbf{f}_1 + \mathbf{f}_3 + \mathbf{f}_5 + \mathbf{f}_7, & \text{underwater mode} \end{cases} \\ \mathbf{T}_2 &= \begin{cases} 0, & \text{air mode} \\ (\mathbf{f}_2 + \mathbf{f}_4 + \mathbf{f}_6 + \mathbf{f}_8)\cos\gamma, & \text{underwater mode} \end{cases} \end{aligned} \tag{5}$$

where $\xi_1 \in \mathbb{R}^3$, and $\xi_2 \in \mathbb{R}^3$ denote the linear position and the velocity of the vehicle with respect to the inertial frame $\mathbf{I}$. m stands for the mass of the vehicle, and g is the gravity constant. $e_1 = [1, 0, 0]^T$ and $e_3 = [0, 0, 1]^T$ are the basis vectors. V indicates the volume of the vehicle. The drag force $C_{D_\xi}\rho D_\xi \xi_2$ is related to the relative velocity between the vehicle and the fluid, where the definition of C_{D_ξ} and D_ξ are similar to C_{D_ϕ} and D_ϕ defined in the subsection *Attitude Dynamics*. In addition, this study does not involve aggressive maneuvers of the vehicle, thus, the coriolis force considered in [14] can be ignored. $\mathbf{T}_1$ and $\mathbf{T}_2$ are the thrust parallel to the basis vectors e_3 and e_1, respectively. In the air mode, most of the rotors' direction is parallel to the basis vector e_3. Therefore, $\mathbf{T}_1$ is the sum of the thrust of all rotors, while $\mathbf{T}_2$ is zero. For the underwater mode, the rotors on the left and right side are tilted. Though the direction of thrust is determined by the tilt angle, it can be decomposed into the component forces in the directions of the e_1 and e_3 vectors. For $\mathbf{T}_1$, it is given by the thrusts $f_i(i = 1, 3, 5, 7)$, and $\mathbf{T}_2$ is related to the thrusts $f_i(i = 2, 4, 6, 8)$ and their tilt angle.

In the motion of the vehicle, buoyancy is only considered in water. For the transition region between water and air, a hybrid system model is proposed in [14]. In this work, the water–air transition is considered as a fast process with a step change in density. Thus, the buoyancy can be defined as a constant, i.e.,

$$F_b = \begin{cases} 0, & \text{air} \\ \rho_w V g, & \text{underwater.} \end{cases} \tag{6}$$

In view of the discussion mentioned above, the following dynamic model of the vehicle is proposed:

$$\begin{aligned} \dot{\Phi}_1 &= \mathbf{P}\Phi_2 \\ J\dot{\Phi}_2 &= -\Phi_2 \times J\Phi_2 - C_{D_\phi}\rho D_\phi \Phi_2 + \boldsymbol{\gamma}\mathbf{T} + \mathbf{Q} \\ \dot{\xi}_1 &= \xi_2 \\ m\dot{\xi}_2 &= \mathbf{T}_1\mathbf{R}e_3 + \mathbf{T}_2\mathbf{R}e_1 + (F_b - mg)e_3 - C_{D_\xi}\rho D_\xi \xi_2. \end{aligned} \tag{7}$$

IV. Controller Design

This section focuses on designing the trajectory control law of the vehicle according to the dynamic model in Section III. In fact, the rotation of the vehicle is much faster than translation in the air, and the translational motion underwater does not require prior rotation. Therefore, a hierarchical controller with time scale separation between the translational and rotational dynamics is designed to realize the motion control of the vehicle in both modes. In this approach, the position of the vehicle is controlled by a virtual control input with the designed angle [14].

A. Trajectory Tracking Control Law

The main challenge of trajectory tracking for the UA/UVs is how to cope with the change of the mediums. The density of water is a thousand times than air, and it changes in distinct water, which makes the parameters of the system uncertain. To overcome this difficulty, an adaptive control law is used, and the problem considered in this work is stated as follows.

Problem 1: Design a control law to make the position vector ξ_1 in the system (7) converges asymptotically to a desired reference ξ_{1d}, i.e.,

$$\lim_{t\to\infty} \xi_1 = \xi_{1d}.$$

To solve this problem, a new virtual control input is desired as

$$\mathbf{u} = \mathbf{T}_1\mathbf{R}e_3 + \mathbf{T}_2\mathbf{R}e_1.$$

Then, the proposed system is simplified as

$$\begin{cases} \dot{\xi}_1 = \xi_2 \\ m\dot{\xi}_2 = \mathbf{u} + (F_b - mg)e_3 - C_{D_\xi}\rho D_\xi \xi_2. \end{cases} \tag{8}$$

Define the error between the desired and the actual state as $\tilde{\xi}_1 \triangleq \xi_{1d} - \xi_1$, and $\tilde{\xi}_2 \triangleq \xi_{2d} - \xi_2$, respectively. The following nonlinear adaptive control law $\mathbf{u}_s$ is designed for the virtual input $\mathbf{u}$:

$$\begin{aligned} \mathbf{u}_s = {} & m\tilde{\xi}_1 + m\ddot{\xi}_{1d} + m\mathbf{K}_1(\dot{\xi}_{1d} - \xi_2) + C_{D_\xi}\hat{\rho}D_\xi\xi_2 \\ & - F_b e_3 + m\mathbf{K}_2\tilde{\xi}_2 + mge_3 \end{aligned} \tag{9}$$

where $\mathbf{K}_1$ and $\mathbf{K}_2 \in \mathbb{R}^{3\times3}$ are diagonal positive definite constant gain matrices, $\xi_{2d} = \dot{\xi}_{1d} + \mathbf{K}_1\tilde{\xi}_1$, and $\hat{\rho} = \frac{1}{m}\int_0^t \tilde{\xi}_2^T C_{D_\xi} D_\xi \xi_2 dt$. Then we can obtain the following result.

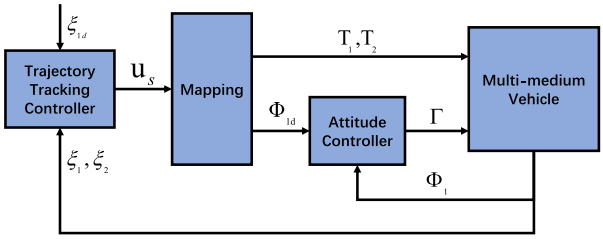

Fig. 4. Block diagram of the overall control scheme.

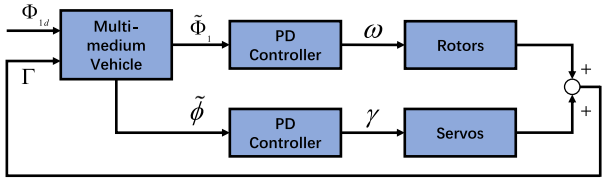

Fig. 5. Block diagram of the attitude control scheme.

Theorem 1: The system (8) asymptotically converges to the desired reference ξ_{1d} if the controller (9) is used, i.e., $\mathbf{u} = \mathbf{u}_s$.

Proof: Define an error variable $\tilde{\rho} \triangleq \rho - \hat{\rho}$, and design a Lyapunov candidate function $\boldsymbol{V}_1$ as

$$\boldsymbol{V}_1 = \frac{1}{2}\tilde{\xi}_1^T\tilde{\xi}_1 + \frac{1}{2}\tilde{\xi}_2^T\tilde{\xi}_2 + \frac{1}{2}\hat{\rho}^2. \tag{10}$$

Note that ρ is a constant, which implies

$$\dot{\tilde{\rho}} = -\dot{\hat{\rho}}.$$

Taking time derivative, applying the control law (8) and substituting $\tilde{\xi}_1$, $\tilde{\xi}_2$, $\tilde{\rho}$ into (10), we have

$$\dot{\boldsymbol{V}}_1 = -\tilde{\xi}_1^T\mathbf{K}_1\tilde{\xi}_1 - \tilde{\xi}_2^T\mathbf{K}_2\tilde{\xi}_2. \tag{11}$$

In view of (11), the function $\dot{\boldsymbol{V}}_1$ is seminegative definite and bounded, then taking into account the Lyapunov-like lemma [27], we obtain $\lim_{t\to\infty}\xi_1 = \xi_{1d}$. ■

B. Mapping of Control Inputs

In order to apply the control law (9) to the vehicle, a mapping of virtual control inputs to the attitude control needs to be established. The overall control scheme block diagram is shown in Fig. 4.

1) Implementation in Air Mode: The reference angles $\Phi_{1d} = [\phi_d \quad \theta_d \quad \psi_d]^T$ are determined by the control inputs $\mathbf{u}_s = [u_{s1} \quad u_{s2} \quad u_{s3}]^T$ given in (9), where

$$\phi_d = -arcsin\frac{u_{s2}}{\mathbf{T}_1} \tag{12}$$

$$\theta_d = arctan\frac{u_{s1}}{u_{s3}\mathbf{T}_1} \tag{13}$$

and ψ_d is set to be zero for simplicity. The thrust $\mathbf{T}_1$ is set to be the modulus of the input vector

$$\mathbf{T}_1 = \sqrt{u_{s1}^2 + u_{s2}^2 + u_{s3}^2}. \tag{14}$$

2) Implementation in Underwater Mode: In this mode, the reference angles ϕ_d and θ_d are set to be zero, and ψ_d is determined by the designed direction of motion. The thrust is divided into horizontal and vertical directions, where the horizontal direction thrust depends on u_{s1} and u_{s2}, and the vertical direction thrust is determined by u_{s3}, i.e.,

$$\mathbf{T}_1 = u_{s3} \tag{15}$$

$$\mathbf{T}_2 = \sqrt{u_{s1}^2 + u_{s2}^2}. \tag{16}$$

C. Attitude Control Scheme

The controller of the existing autopilot [28] with modifications is used for the air mode. For the underwater mode, the linkage control scheme for the speed and the tilt angle of the rotors is proposed, which is shown in Fig. 5.

1) Rotor Tilt Angle Control: The tilt angle determines the component force generated by the thrust in the roll direction. Let ϕ_d be the desired roll angle, then the roll angle error $\tilde{\phi}$ can be expressed as

$$\tilde{\phi} = \phi - \phi_d \tag{17}$$

and the rotor tilt angle is given by the PD controller

$$\gamma = -k_{\phi,p}\tilde{\phi} - k_{\phi,d}\dot{\tilde{\phi}} \tag{18}$$

where $k_{\phi,p}$ and $k_{\phi,d}$ are the controller gains.

2) Rotor Speed Control: Define Φ_{1d} as the desired angle, then the angle error is $\tilde{\Phi}_1 = \Phi_1 - \Phi_{1d}$. The attitude control law is given by the PD controller

$$\mathbf{T} = -\mathbf{K}_{\Phi_1,p}\tilde{\Phi}_1 - \mathbf{K}_{\Phi_1,d}\dot{\tilde{\Phi}}_1 \tag{19}$$

where $\mathbf{K}_{\Phi_1,p}$ and $\mathbf{K}_{\Phi_1,d}$ are the controller gain matrices. The mapping of thrust to rotor speed is given in (4).

Remark 1: In the underwater mode, the initial tilt angle of the rotors setting of 0° results a delay of the input torque in the roll direction. Because the rotors need to be turned at a large angle to get sufficient force, the controller is unable to modify the attitude in time in the presence of external disturbances. Fortunately, this setting is feasible underwater due to the strong drag in the water, as the drag reduces the effect of external disturbances on the attitude dynamics.

V. Simulation Validation

Simulations are performed through the *MATLAB Simulink*. This section consists of two parts. The adaptive control law is validated in Section V-A. Moreover, the effectiveness of our proposed controller in different environments is verified in Section V-B.

A. Validation of the Adaptive Control Law

In this subsection, a set of trajectory tracking experiments are designed. Define $z = 0$ as the intersection of water and air, and the initial position of the vehicle is the origin of the coordinate axis. The tasks include: 1) diving 2 m underwater in the z-direction; 2) advancing 4 m in the y-direction; 3) advancing 4 m in the x-direction; 4) rising 2 m up to the water surface in

TABLE I
SIMULATION PARAMETERS

$m[kg]$	$V[cm^3]$	J	g
5	2000	69	9.8
C_{D_ξ}	C_{D_ϕ}	$\mathbf{K}_1$	$\mathbf{K}_2$
0.01	0.01	$[0.3, 0.3, 0.6]$	$[5, 5, 8]$
$\mathbf{K}_{\Phi_1,p}$	$\mathbf{K}_{\Phi_1,d}$	$k_{\phi,p}$	$k_{\phi,d}$
$[0.5, 0.5, 10]$	$[3, 3, 12]$	0.1	0.3

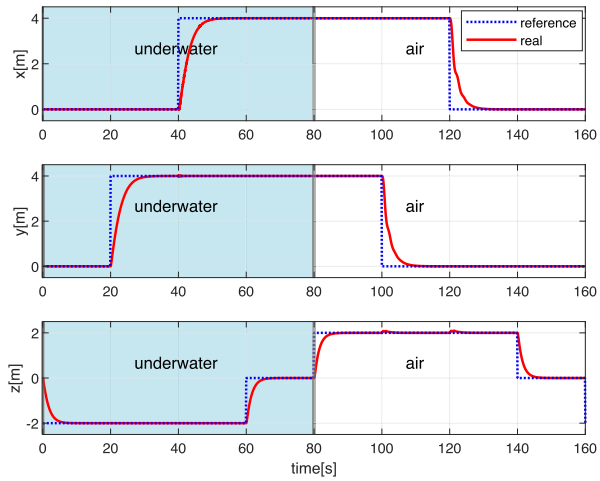

Fig. 6. Target trajectory and the actual trajectory of the vehicle.

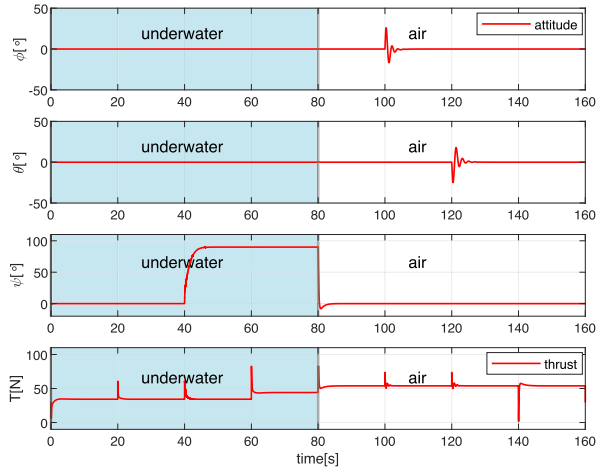

Fig. 7. Attitude of vehicle and the thrust input.

the z-direction; 5) flying to a height of 2 m in the z-direction; 6) retreating 4 m in the y-direction; 7) retreating 4 m in the x-direction; 8) descending 2 m in the z-direction back to the origin. The trajectory tracking simulation is cascaded with the attitude control simulation. Table I gives the parameters used in the simulations, the results are shown in Figs. 6–8.

Fig. 6 depicts the target trajectory and the actual trajectory of the vehicle, where the blue area represents the vehicle operating underwater. As shown in the figure, the vehicle starts to fly from the water surface to the air at time 80 s. The simulation shows that the underwater dynamics are slightly slower than the air, as

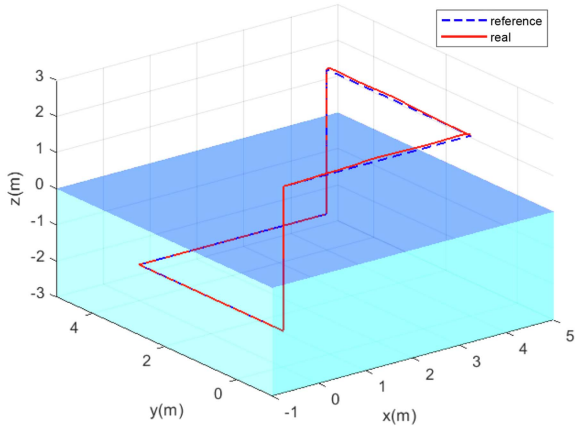

Fig. 8. 3-D representation of the mission.

the drag in the water is much larger than in the air. However, the compensation term in the control law has reduced the gap as much as possible. In addition, it can be observed that the vehicle altitude is affected during translational motion in the air mode due to the coupling of translational and rotational dynamics (see time 100 and 120 s). This phenomenon does not occur in the underwater mode because the altitude control is independent.

Fig. 7 shows the attitude variations of the vehicle during the mission (top three) and the total thrust output of the rotors (bottom), respectively. From this figure, the roll and pitch angle of the vehicle are barely changed underwater because the direction of motion is determined by the yaw angle. The bottom plot in Fig. 7 depicts the total thrust during the mission, the maximum thrust input in the simulation is limited to 1.5 times the vehicle weight to better simulate the real situation. It can be observed that the average thrust underwater is less than that in the air. As a result, due to the fact that buoyancy overcomes part of the vehicle weight, the underwater energy consumption is lower.

Finally, Fig. 8 shows the complete task in a 3-D representation, where the light blue area indicates water and the dark blue plane indicates the boundary between water and air. The simulation result represents that the control scheme enables the vehicle to track on the designed trajectory in both mediums.

B. Performance of Controller in Different Environments

To evaluate the effectiveness of the proposed controller in various environments, we conduct two trajectory tracking experiments.

In the experiments, we focus on the underwater altitude control and the reference trajectory is a step trajectory. The first experiment is performed in the lake ($\rho = 1000\,\text{kg/m}^3$), and the controller gains are adjusted to achieve the desired tracking performance. Without changing the controller gains, the second experiment is conducted in the sea ($\rho = 1025\,\text{kg/m}^3$). The performance of the adaptive control law in different environments is shown in Fig. 9, which indicates that the performance of the proposed controller is minimally affected by variations in density.

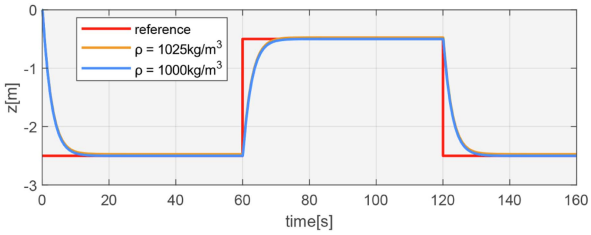

Fig. 9. Trajectory tracking performance of the adaptive control law.

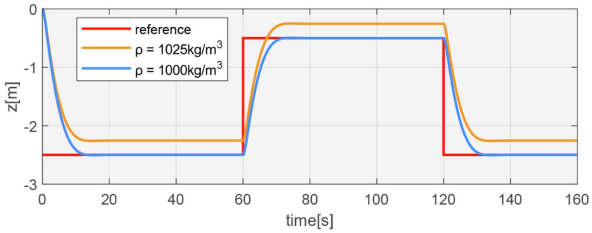

Fig. 10. Trajectory tracking performance of the feedback linearization control law.

To compare our proposed method with the existing feedback linearization control law [14], the same experiments are performed. To enhance the intuitiveness of the results, its desired trajectory tracking performance is adjusted to be close to the condition using the adaptive control law. The performance of the feedback linearization control law is shown in Fig. 10, which shows that it exists a steady-state error when the density is altered. Therefore, the proposed control law possesses greater versatility in different environments compared to the feedback linearization control law.

VI. Experimental Validation

In this section, some experiments are performed to verify the performance of the designed vehicle, including the in-water and out-water flight tests.

A. Experimental Setup

The designed vehicle is equipped with eight rotors, each rotor contains a 900-kV 2814 BLDC motor and a (10 × 7)-in two-blade propeller. The speed and the tilt angle of the rotors are, respectively, controlled by the ESCs and servos via the PWM signals given by the autopilot. The motors and servos are separately powered by a 5000-mAh 4 s and a 550-mAh 2 s Li-ion battery, the autopilot is powered by the 4 s battery through a BEC. The ACFLY open source flight controller is used for the autopilot in this platform, which contains the inertial measurement unit required for the experiment. The original flight controller has been replaced with the custom code. The manual operation commands are sent from the transmitter to the receiver, then transmitted to the autopilot via the SBUS serial communication protocol. The tasks and data are sent/received by the ground station via wireless signal transmission. To sum up, the overview of the system is shown in Fig. 11.

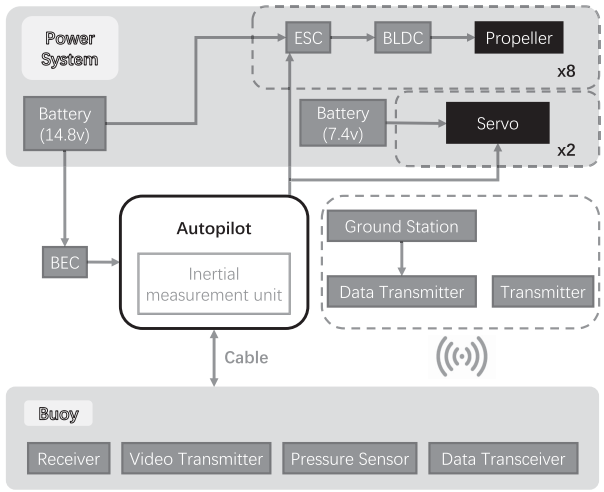

Fig. 11. Overview of the Puffin vehicle platform.

Underwater robots usually use cable communication to guarantee the stability of communication and data transmission rate. However, the weight of the cable affects the control of the vehicle when sailing a long distance. For this reason, we use a combination of cable and wireless communication. The cable consists of a 2.4 g receiver antenna, a 5.8 g video transmitter antenna, a two-way telemetry link, and a water sensor signal line, for a total of four wires. A buoy is attached to the end of the cable to ensure that the communication antenna is located in the air for wireless communication. The top of the vehicle is equipped with a cable reel device to store the cable, the length of the released cable is adjusted according to the diving depth of the platform. The pressure sensor is carried on the buoy to judge whether it is floating on the water surface. The length of the released cable is changed if the buoy is close to sink.

Finally, the water-sensitive electronic components of the vehicle are sealed in a waterproof pressure vessel. However, placing the ESC in the waterproof pressure vessel is not conducive for heat dissipation since it is a heat-generating component. Therefore, it is wrapped with silicone for waterproof treatment and fixed on the airframe.

B. Preliminary Experiments

The position control of the vehicle is done manually due to the lack of estimation of the vehicle's position underwater. Although the GPS can be placed on the buoy, the position of the buoy relative to the vehicle is uncertain, thus, the accuracy of position estimation cannot be guaranteed. The acoustic sensors used for underwater localization are too heavy to be loaded by a small vehicle. Thus, we only test the attitude retention capability and transition performance of the vehicle in both media. To ensure the sinking ability underwater, the vehicle is designed to be heavier than the buoyancy. Define the resultant force F_{sum} as the sum of the thrust provided by the front and rear rotors and the buoyancy. $\mathcal{T}$ is the throttle value of the front and rear rotors. The position control of the vehicle in z-coordinate is defined in the following three modes. 1) *Uplift Mode:* The vehicle

TABLE II
EXPERIMENTAL PARAMETERS

Mode	$\mathcal{T}$	$\mathbf{K}_{\Phi_1,p}$	$\mathbf{K}_{\Phi_1,d}$	$k_{\phi,p}, k_{\phi,d}$
Uplift mode	10%			
Maneuver mode	7%	$[40, 40, 10]$	$[0, 40, 0]$	$6, 0$
Sink mode	5%			

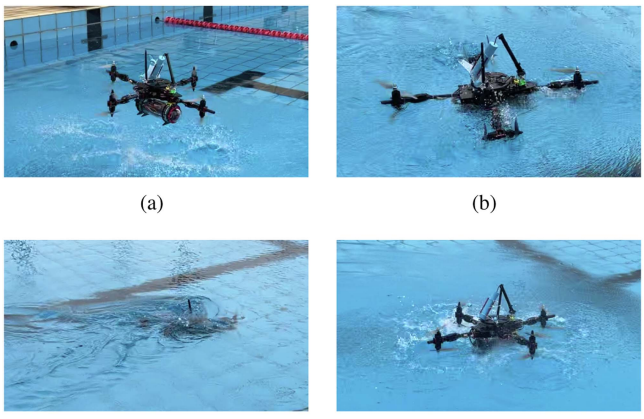

(a) (b) (c) (d)

Fig. 12. Sequence of pictures of Puffin platform in the test.

exhibits positive buoyancy ($F_{sum} > mg$). 2) *Maneuver Mode:* The vehicle exhibits neutral buoyancy ($F_{sum} \approx mg$). 3) *Sink Mode:* The vehicle exhibits negative buoyancy ($F_{sum} < mg$). The main flight parameters of the experimental platform are summarized in Table II.

The test for transition is divided into four phases: 1) landing from the air to the water surface; 2) sinking from the water surface until it is fully submerged; 3) floating to the water surface; 4) taking off from the water surface to the air. Fig. 12 shows an image sequence illustrating the test. The transition strategy is to switch the modes, where the vehicle switches from air mode to uplift mode while in-water transition and switches in reverse for out-water transition.

To further verify the effectiveness of the proposed attitude methods, we designed some experiments to test the response of the attitude controller. Due to the lack of localization, the altitude control of the vehicle needs to be manually operated. In order to exclude the influence of manual operation for the experiments, we set the mode to uplift mode to keep the vehicle floating on the water surface. Under this setup, we tested the attitude response of the platform in both the roll and pitch axes. The target angles were set to be 20° and they were given in the form of step signals in the experiments. For comparison, the same settings were used for the experiments in the air.

The attitude response of the attitude controller in both mediums is shown in Fig. 13, where the red line represents the target angle and the blue line is the measured value of the angle. The results reveal that the attitude response in water is much slower than in air, and it has a large steady-state error. These are caused by the strong resistance of the water. Moreover, there is a slight oscillation present in the measurement of the attitude while the vehicle was in the water. As a portion of the propellers were in

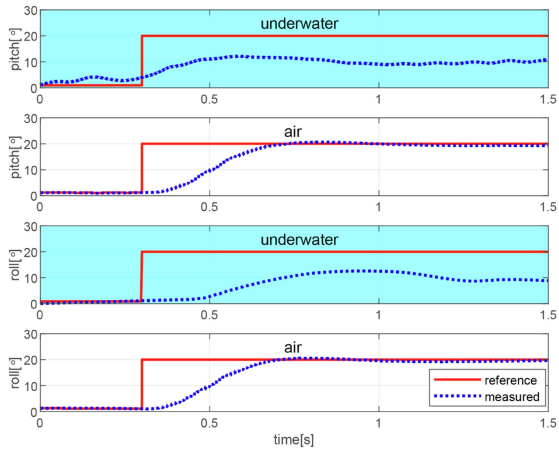

Fig. 13. Flight attitude of Puffin platform in the test.

the air while the rest were submerged in water, the difference in medium results in the interference.

All in all, the controller meets the expected results in the preliminary experiments. In the future work, experiments in water should be conducted with the vehicle fully submerged and the attitude controller requires further improvement to enhance performance.

VII. CONCLUSION

In this article, we developed a morphable UA/UV, the Puffin platform. The novel vehicle consisted of a tilting mechanism. The controllers were proposed based on the modeling of this system and their performance was verified by simulations. In addition, some preliminary experiments were established. The proposed attitude control method achieved the flight control and transition in the two mediums. The position control of the platform was manually operated, which was currently limited by the underwater localization. Future work would include adding sensors for underwater localization and verifying the position controller through the platform.

REFERENCES

[1] T. Yang, Z. Jiang, R. Sun, N. Cheng, and H. Feng, "Maritime search and rescue based on group mobile computing for unmanned aerial vehicles and unmanned surface vehicles," *IEEE Trans. Ind. Inform.*, vol. 16, no. 12, pp. 7700–7708, Dec. 2020.

[2] G. Winkelmaier, R. Battulwar, M. Khoshdeli, J. Valencia, J. Sattarvand, and B. Parvin, "Topographically guided UAV for identifying tension cracks using image-based analytics in open-pit mines," *IEEE Trans. Ind. Electron.*, vol. 68, no. 6, pp. 5415–5424, Jun. 2021.

[3] F. Lin, X. Dong, B. M. Chen, K.-Y. Lum, and T. H. Lee, "A robust real-time embedded vision system on an unmanned rotorcraft for ground target following," *IEEE Trans. Ind. Electron.*, vol. 59, no. 2, pp. 1038–1049, Feb. 2012.

[4] L. Yu, G. He, X. Wang, and S. Zhao, "Robust fixed-time sliding mode attitude control of tilt trirotor UAV in helicopter mode," *IEEE Trans. Ind. Electron.*, vol. 69, no. 10, pp. 10322–10332, Oct. 2022.

[5] V. P. Bacheti, A. S. Brandão, and M. Sarcinelli-Filho, "Path-following with a UGV-UAV formation considering that the UAV lands on the UGV," in *Proc. Int. Conf. Unmanned Aircr. Syst.*, 2020, pp. 488–497.

[6] N. Shirakura, T. Kiyokawa, H. Kumamoto, J. Takamatsu, and T. Ogasawara, "Semi-automatic collection of marine debris by collaborating UAV and UUV," in *Proc. IEEE 4th Int. Conf. Robot. Comput.*, 2020, pp. 412–413.

[7] E. Sollesnes et al., "Towards autonomous ocean observing systems using miniature underwater gliders with UAV deployment and recovery capabilities," in *Proc. IEEE/OES Auton. Underwater Veh. Workshop*, 2018, pp. 1–5.
[8] H. J. T. Suh, X. Xiong, A. Singletary, A. D. Ames, and J. W. Burdick, "Energy-efficient motion planning for multi-modal hybrid locomotion," in *Proc. IEEE/RSJ Int. Conf. Intell. Robots Syst.*, 2020, pp. 7027–7033.
[9] K. Kim, P. Spieler, E.-S. Lupu, A. Ramezani, and S.-J. Chung, "A bipedal walking robot that can fly, slackline, and skateboard," *Sci. Robot.*, vol. 6, no. 59, 2021, Art. no. eabf8136.
[10] X. Yang, T. Wang, J. Liang, G. Yao, and M. Liu, "Survey on the novel hybrid aquatic-aerial amphibious aircraft: Aquatic unmanned aerial vehicle (AquaUAV)," *Prog. Aerosp. Sci.*, vol. 74, pp. 131–151, 2015.
[11] A. C. Horn, P. M. Pinheiro, R. B. Grando, C. B. da Silva, A. A. Neto, and P. L. Drews, "A novel concept for hybrid unmanned aerial underwater vehicles focused on aquatic performance," in *Proc. Latin Amer. Robot. Symp. Braz. Symp. Robot. Workshop Robot. Edu.*, 2020, pp. 1–6.
[12] H. Alzu'bi, I. Mansour, and O. Rawashdeh, "Loon Copter: Implementation of a hybrid unmanned aquatic-aerial quadcopter with active buoyancy control," *J. Field Robot.*, vol. 35, no. 5, pp. 764–778, 2018.
[13] D. Canelon-Suarez, Y. Wang, and N. Papanikolopoulos, "Omnibot: A small versatile robotic platform capable of air, ground, and underwater operation," in *Proc. Int. Conf. Unmanned Aircr. Syst.*, 2020, pp. 1742–1747.
[14] D. A. M. Ravell, M. M. Maia, and F. J. Diez, "Modeling and control of unmanned aerial/underwater vehicles using hybrid control," *Control Eng. Pract.*, vol. 76, pp. 112–122, 2018.
[15] J. Moore, A. Fein, and W. Setzler, "Design and analysis of a fixed-wing unmanned aerial-aquatic vehicle," in *Proc. IEEE Int. Conf. Robot. Autom.*, 2018, pp. 1236–1243.
[16] W. Stewart et al., "Design and demonstration of a seabird-inspired fixed-wing hybrid UAV-UUV system," *Bioinspiration Biomimetics*, vol. 13, 2018, Art. no. 056013.
[17] Y. H. Tan, B. H. Liew, X. Liu, and B. M. Chen, "Wing design studies for small submersible-launched UAVs," in *Proc. IEEE 14th Int. Conf. Control Autom.*, 2018, pp. 350–354.
[18] H. Gu, X. Lyu, Z. Li, S. Shen, and F. Zhang, "Development and experimental verification of a hybrid vertical take-off and landing (VTOL) unmanned aerial vehicle (UAV)," in *Proc. Int. Conf. Unmanned Aircr. Syst.*, 2017, pp. 160–169.
[19] J. Autenrieb, H.-S. Shin, and M. Bacic, "Development of a neural network-based adaptive nonlinear dynamic inversion controller for a tilt-wing VTOL aircraft," in *Proc. Workshop Res., Educ. Develop. Unmanned Aerial Syst.*, 2019, pp. 44–52.
[20] D. Lu, C. Xiong, Z. Zeng, and L. Lian, "A multimodal aerial underwater vehicle with extended endurance and capabilities," in *Proc. Int. Conf. Robot. Autom.*, 2019, pp. 4674–4680.
[21] Y. H. Tan and B. M. Chen, "Thruster allocation and mapping of aerial and aquatic modes for a morphable multimodal quadrotor," *IEEE/ASME Trans. Mechatron.*, vol. 25, no. 4, pp. 2065–2074, Aug. 2020.
[22] S. Zhao, H. Zhang, P. Wang, L. Nogueira, and S. Scherer, "Super odometry: IMU-centric LiDAR-visual-inertial estimator for challenging environments," in *Proc. IEEE/RSJ Int. Conf. Intell. Robots Syst.*, 2021, pp. 8729–8736.
[23] H. Wang, S. Zhang, X. Zhang, X. Zhang, and J. Liu, "Near-optimal 3-D visual coverage for quadrotor unmanned aerial vehicles under photogrammetric constraints," *IEEE Trans. Ind. Electron.*, vol. 69, no. 2, pp. 1694–1704, Feb. 2022.
[24] M. S. M. Aras et al., "Analysis of integrated sensors for unmanned underwater vehicle application," in *Proc. IEEE Int. Conf. Underwater System Technol.: Theory Appl.*, 2016, pp. 224–229.
[25] Z. Zuo, C. Liu, Q.-L. Han, and J. Song, "Unmanned aerial vehicles: Control methods and future challenges," *IEEE/CAA J. Automatica Sinica*, vol. 9, no. 4, pp. 601–614, Apr. 2022.
[26] R. Mahony, V. Kumar, and P. Corke, "Multirotor aerial vehicles: Modeling, estimation, and control of quadrotor," *IEEE Robot. Autom. Mag.*, vol. 19, no. 3, pp. 20–32, Sep. 2012.
[27] R. Mahony, T. Hamel, and J.-M. Pflimlin, "Nonlinear complementary filters on the special orthogonal group," *IEEE Trans. Autom. Control*, vol. 53, no. 5, pp. 1203–1218, Jun. 2008.
[28] L. Meier, D. Honegger, and M. Pollefeys, "PX4: A node-based multithreaded open source robotics framework for deeply embedded platforms," in *Proc. IEEE Int. Conf. Robot. Autom.*, 2015, pp. 6235–6240.

Hongxia Rao received the B.S. degree in electronic science and technology from Nanchang Hangkong University, Nanchang, China, in 2007, the M.S. degree in communication and information system from the Nanjing University of Science and Technology, Nanjing, China, in 2009, and the Ph.D. degree in control science and engineering from the Guangdong University of Technology, Guangzhou, China, in 2019.

She is currently a Lecturer with the School of Automation, Guangdong University of Technology. Her research interests include networked control systems, Markov jump systems, and neural networks.

Lijie Xie received the B.S. degree in microelectronics science and engineering in 2021 from the Guangdong University of Technology, Guangzhou, China, where he is currently working toward the M.S. degree in control engineering.

His research interests include UAV modeling and control.

Jiapeng Yang received the B.S. degree in electronic information science and technology in 2021 from the Guangdong University of Technology, Guangzhou, China, where he is currently working toward the M.S. degree in control science and engineering.

His research interests include robot motion control and motor vector control.

Yong Xu (Member, IEEE) received the B.S. degree in information engineering from Nanchang Hangkong University, Nanchang, China, in 2007, the M.S. degree in control science and engineering from Hangzhou Dianzi University, Hangzhou, China, in 2010, and the Ph.D. degree in control science and engineering from Zhejiang University, Hangzhou, China, in 2014.

He is currently a Professor with the School of Automation, Guangdong University of Technology, Guangzhou, China. His research interests include PID control, networked control systems, state estimation, and positive systems.

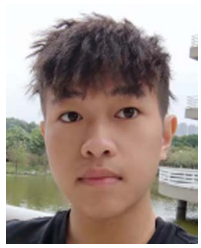

Weijun Lv received the B.S. degree in automation from the Guangdong University of Technology, Guangzhou, China, in 2020, where he is currently working toward the M.S. degree in control science and engineering.

His research interests include networked systems and state estimation.

Zongkai Zheng received the B.S. degree in mechatronic engineering from the Guangdong University of Technology, Guangzhou, China, in 2021. He is currently working toward the M.S. degree in mechanical engineering from the Harbin institute of Technology (ShenZhen), Shenzhen, China.

His research interest includes cable-driven parallel robot.

Yihui Deng received the B.S. degree in mechanical engineering and automation from the Guangdong University of Technology, Guangzhou, China, in 2021. He is currently working toward the M.S. degree in electronic information engineering with the University of Electronic Science and Technology of China, Sichuan, China.

His research interest includes UAV vision positioning system.

Haotian Guo received the B.S. degree in data science and Big Data technology from the Guangdong University of Technology, Guangzhou, China, in 2022.